JGR Solid Earth

RESEARCH ARTICLE
10.1029/2024JB029057

Permeability Development During Fault Growth and Slip in Granite

Franciscus M. Aben[1,2], **Ado Farsi**[1], **and Nicolas Brantut**[1]

[1]Department of Earth Sciences, University College London, London, UK, [2]TNO Applied Geosciences, Utrecht, The Netherlands

Key Points:

- Average permeability changed a factor 100 during loading toward peak stress, and by a factor 3 during fault growth
- During fault growth, local permeability heterogeneities up to a factor 8 are correlated to the growth of the fracture network
- With continuing slip after fault completion, the transmissivity remains stable whilst the fault continues to dilate

Correspondence to:
F. M. Aben,
frans.aben@tno.nl

Citation:
Aben, F. M., Farsi, A., & Brantut, N. (2024). Permeability development during fault growth and slip in granite. *Journal of Geophysical Research: Solid Earth*, *129*, e2024JB029057. https://doi.org/10.1029/2024JB029057

Received 22 MAR 2024
Accepted 4 DEC 2024

Author Contributions:
Conceptualization: Franciscus M. Aben, Nicolas Brantut
Formal analysis: Ado Farsi, Nicolas Brantut
Funding acquisition: Nicolas Brantut
Investigation: Franciscus M. Aben
Methodology: Franciscus M. Aben, Nicolas Brantut
Software: Nicolas Brantut
Writing – original draft: Nicolas Brantut
Writing – review & editing: Franciscus M. Aben, Ado Farsi

Abstract In tight crystalline rocks faults are known to be substantially more hydraulically conductive than the rock matrix. However, most of our knowledge relies on static measurements, or before/after failure data sets. The spatio-temporal evolution of the permeability field during faulting remains unknown. Here, we determine at which stage of faulting permeability changes most, and the degree of permeability heterogeneity along shear faults. We conducted triaxial deformation experiments in intact Westerly granite, where faulting was stabilized by monitoring acoustic emission rate. At repeated stages during deformation and faulting we paused deformation and imposed macroscopic fluid flow to characterize the overall permeability of the material. The pore pressure distribution was measured along the prospective fault to estimate apparent hydraulic transmissivity, and propagation of the macroscopic shear fault was monitored by locating acoustic emissions. We find that average permeability increases dramatically (by two orders of magnitude) with increasing deformation up to peak stress, where the fault is not yet through-going. Post-peak stress, overall permeability increases by a factor of three. However, at this stage we observed local heterogeneities in permeability by up to factors of eight, ascribed to a partially connected fracture network. This heterogeneity decreases with fault completion at residual shear stress. With further slip on the newly formed fault, the average hydraulic transmissivity remains mostly stable. Our results show that permeability enhancement during shear rupture mostly occurs ahead of the rupture tip, and that strongly heterogeneous permeability patterns are generated in the fault cohesive zone due to partial fracture connectivity.

Plain Language Summary The Earth's crust is comprised of low porosity rock, therefore flow of fluids is mostly limited to fractures and faults. This is shown by permeability measurements that tell how well fluids flow through intact crustal rock and through their faulted and fractured counterparts. However, how permeability changes during the creation of a fault in intact rock is not well documented. Here, in a laboratory experiment we measured how well fluids flow prior, during, and after the growth of a fresh fault in granite. During the experiment, the location of the growing fault was tracked by capturing the micro-earthquakes called acoustic emissions. Miniature pore pressure sensors placed on the (prospective) fault plane were then used to derive a local permeability. The results show that the largest change in permeability, of a factor 100, took place during deformation prior to the onset of fault growth. This increase is due to opening of small cracks distributed in the intact rock. Once the fault started growing, permeability of the entire sample increased by a factor 3. Within the growing fault tip, we observed strong spatial variations in permeability of up to a factor 8. Once completed, the fluid flow ability of the fault remained stable. Our results show that the largest change in permeability is just before and at the onset of fault growth.

1. Introduction

Fluid flow in the Earth's crust is controlled by the connectivity and hydraulic transmissivity of fractures. In bulk rock material, fluids flow through a connected network of microcracks and pores. In crystalline basement rocks such as granite, the resulting permeability of the rock matrix is typically low, of the order of 10^{-19} m^2 or less (e.g., Brace et al., 1968). At crustal scale, fluid flow is focused along fault zones, which tend to be orders of magnitude more permeable than intact rocks (e.g., Townend & Zoback, 2000).

How does permeability and fluid flow patterns evolve during the formation and growth of fault zones? This fundamental problem impacts a variety of topics that require information on fluid flow in active fault zones, for example, the dynamics of ruptures in the presence of fluids (e.g., Brantut, 2021; Garagash & Rudnicki, 2003) and the dynamics of earthquake swarms in the crust (e.g., De Barros et al., 2020; Ross & Cochran, 2021; Ross

et al., 2020). Deformation of initially intact granite in the brittle regime (under triaxial conditions) leads to a progressive increase in permeability of the rock matrix, typically by a factor of 3 at stresses up to 80% of the failure strength (Zoback & Byerlee, 1975). At stresses reaching the failure strength permeability increases dramatically, by two to three orders of magnitudes (Farquharson et al., 2016; Kluge et al., 2021; Mitchell & Faulkner, 2008). This permeability increase is closely linked to the formation of a shear fault, which becomes the main flow path for fluids. There are thus two combined effects of brittle deformation: a modest bulk increase in permeability associated to distributed dilatant cracking, and a large localized increase in permeability associated to the formation of a shear fault. In the tests reported by Mitchell and Faulkner (2008) and Kluge et al. (2021), the formation of the fault is very sudden, and only the average permeability of the sample is measured: while extremely valuable, these observations do not allow us to determine the localized nature of the flow and the possible complications due to development of heterogeneity in the rock.

Indeed, the formation of shear faults in initially intact rock involves the growth and linkage of an ensemble of microcracks in a fault "nucleus," the propagation of the shear fracture which concentrates stress, and microcrack damage, at its tips, and slip on the newly formed fault (Lockner et al., 1991; Zang et al., 2000). These processes produce a heterogeneous fault structure with a damage zone that is evidenced by a strong decrease in elastic wave velocity near the fault (Aben et al., 2019). We thus expect that fluid transport properties also become heterogeneous, but it is not clear if the structure that becomes more conductive is the fault plane, the damage zone, or the process zone ahead of the rupture tip.

The evolution of permeability with on-going slip is also difficult to assess a priori. While all existing data on initially intact low porosity rock show a dramatic increase in permeability due to the formation of a fault, there are extensive measurements on saw cuts and artificial fault gouges that show a clear decrease in permeability with increasing slip, sometimes by up to three orders of magnitude (Crawford et al., 2008; Rutter & Mecklenburgh, 2018; Teufel, 1987; Zhang et al., 1999; Zhang & Tullis, 1998). The state of consolidation of the fault gouge, together with wear processes, play a key role in setting the evolution of permeability. Recent experimental work by Im et al. (2018) also show a time-dependence of the permeability evolution with on-going slip: "fresh" saw-cuts shows a decrease in permeability at the onset of slip, but the trend is reversed when slip occurs after an extended "hold" time that allows compaction of the fault material. Measuring permeability evolution in spontaneously fractured rock is thus an attractive way to alleviate potential biases due to artificial preconsolidation.

Kiyama et al. (1996) characterized fully the evolution of permeability throughout the failure process in granite, including the "postpeak region," that is, from the onset of faulting to frictional slip on the newly formed fault. They report a continuous increase in permeability with increasing radial deformation, a proxy for dilational strain. In the post-peak region, permeability increases steadily, and the increase seems to be less pronounced once residual friction is achieved. This early work was conducted at a very small effective confining pressure of 5 MPa, and it is not clear if these results hold when rocks are under more elevated pressure.

The goal of this paper is to determine the spatiotemporal evolution of permeability during shear fracture growth and fault slip in granite, under upper crustal conditions. We deformed Westerly granite samples under triaxial conditions, and paused the shear failure process at multiple stages. We tracked rupture growth using acoustic emission locations, and estimated local permeability at different positions along the fault using an array of fluid pressure transducers recording pore pressure gradients during steady flow.

2. Methods

Three experiments were conducted, on samples WGMS2, WGMS3, and WGMS4. The data from the experiments on the former two samples could not be used entirely due to technical issues detailed below. Nonetheless, the data acquired before these technical issues is used in this manuscript. All data from sample WGMS4 is presented in this manuscript. When describing experimental results, these will be from sample WGMS4 unless otherwise stated.

2.1. Sample Material and Geometry

We chose Westerly granite as sample material, because of the extensive prior knowledge of this rocks' mechanical and hydraulic properties (e.g., Mitchell & Faulkner, 2008; Zoback & Byerlee, 1975). We prepared cylindrical samples of 100 mm in length and 40 mm in diameter from a homogeneous block of granite containing no visible

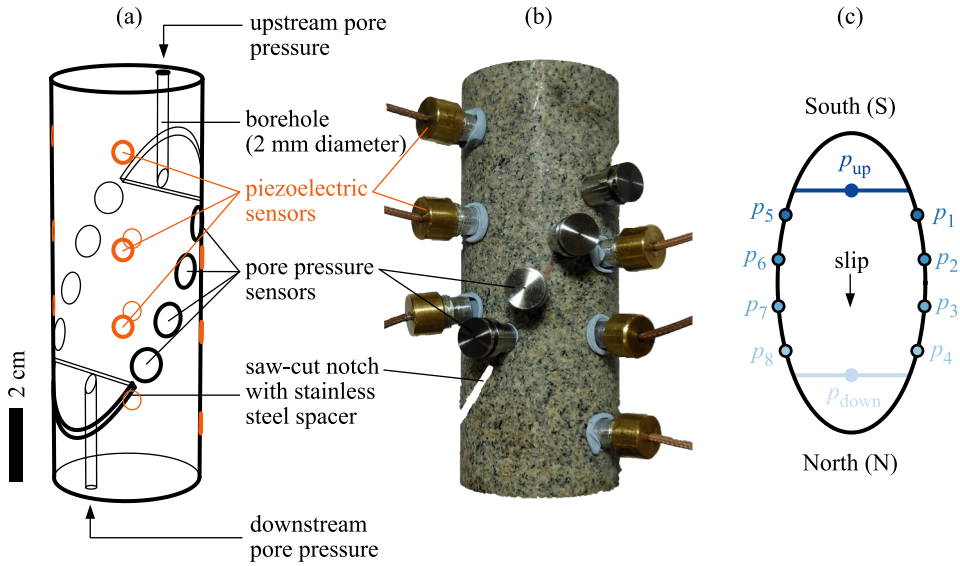

Figure 1. Schematic of the sample geometry and sensor arrangement.

preexisting fracture or vein. In order to favor the location of the eventual shear failure plane along a known path, we cut a pair of notches at 30° from the loading axis on opposite sides of the samples. The notches were 1.5 mm wide, and 15 mm deep. This leaves 50 mm of intact rock to be ruptured between the notches. Small 2 mm diameter boreholes were drilled from the sample ends so that each notch would be hydraulically connected to the up- and downstream boundaries (Figure 1). In sample WGMS4, to prevent the collapse of the notches under pressure, we filled them with stainless steel spacers that were machined to leave a gap between the borehole and the notch tip. This gap ensured good hydraulic connectivity between the extremities of the prospective fault zone and the up- and downstream boundaries where fluid pressure was imposed. In two of our early experiments (on samples WGMS2 and WGMS3), we used Teflon as filler material for the notches, in an attempt to minimize the contribution of the filling material to fault zone friction. However, it became apparent that Teflon could not be prevented from creeping into the borehole and eventually obstructed it nearly completely. Although these experiments could not be used beyond that point for fluid flow analysis, we will present some of the data collected before full borehole blockage, as well as net fluid volume changes which were not impacted by the issue.

2.2. Sample Instrumentation

The samples were jacketed in a 3 mm thick nitrile sleeve equipped with (a) an array of 12 piezoelectric transducers, and (b) an array of 6–8 miniature fluid pressure transducers.

The piezoelectric transducers are polarized normal to the sample surface. They are uncalibrated, with a resonant frequency of the order of 250 kHz. The transducers were bonded with cyanoacrylate in direct contact with the rock, and sealing with the jacket was achieved with epoxy. The sensor locations were arranged to maximize coverage of the entire sample volume, with 6 transducers located on each side of the eventual failure plane (Figure 1). All transducers were preamplified to 40 dB in the 100 kHZ to 1 MHz frequency range, and the amplified signals were recorded continuously at 10 MHz with 16 bits dynamic range over a full scale of 5 V. In addition, the transducers were also used as ultrasonic sources to measure time-of-flight between sensor pairs at repeated intervals during the experiments. During these surveys, a set of 6, 1 MHz, 250 V pulses were sent to each sensor, and the signals received on the remaining sensors were stacked and recorded at 50 MHz with 12 bit dynamic range in separate digital oscilloscopes.

A complete description of the pore pressure transducers can be found in Brantut (2020); Brantut and Aben (2021). They consist of a stainless steel stem positioned in direct contact with the rock, with a 0.4 mm diameter conduit connecting the sample pore space to a 0.2 mm thick circular cavity isolated from the confining medium by a steel cap. The cap is mounted with a diaphragm strain gauge that measures the cap distorsion in response to differential changes in confining and pore fluid pressure. The pressure measurements have a precision of the order of

0.06 MPa (Brantut, 2021). The pressure transducers were arranged to maximize the detection of pressure gradients along the failure plane, with 4 sensors positioned in line with the eventual fault on each side of the sample (Figure 1). Each transducer was connected (via high pressure leadthroughs) to a bridge amplifier, and the amplified signals were recorded at 1 Hz.

2.3. Deformation Tests

The jacketed samples were saturated with distilled water and deformed in an oil-medium triaxial apparatus. The confining pressure was measured with a pressure transducer positioned at the inlet of the confining oil input into the pressure vessel, and controlled by an electric pump to an accuracy of 0.8 MPa. The pore fluid pressure was imposed at both ends of the sample by a servo-hydraulic intensifier, and measured at the intensifier outlet by a pressure transducer. Changes in intensifier volume were measured by tracking the displacement of the intensifier piston, with a precision of around 0.005 cc. Intensifier volume data were used to determine (a) the pore volume change of the sample when pore pressure is equilibrated throughout the sample volume, and (b) flow rate across the sample during permeability measurements. Axial load was imposed via a piston driven by a servo-hydraulic ram. Load was measured with an external load cell, corrected from piston friction (measured prior to hit point) and differential stress on the sample was computed by dividing the corrected load by the sample nominal surface area. Axial shortening was measured by a pair of linear variable differential transformers tracking the piston motion outside the pressure vessel, and corrected for the elastic distortion of the loading column. All mechanical and pore pressure data were recorded at 1 Hz.

The samples were initially pressurized hydrostatically up to a target 85 MPa confining pressure, while pore pressure was kept constant at 5 MPa. After a period of equilibration, axial load was then initially applied at constant shortening rate equivalent to 10^{-6} s^{-1} strain rate. When the peak stress was approached and throughout the post-peak phase, we regularly unloaded and re-loaded the sample to prevent uncontrolled acceleration of deformation and dynamic failure, in the same manner as described in Aben et al. (2019). In addition, at regular intervals throughout the experiment flow-through tests were conducted. To do so, we paused deformation during unloading cycles where the sample did not deform any further, established by monitoring the acoustic emission (AE) rate. We then waited for full internal pore pressure equilibration and a stable pore volume. Once achieved, we vented the downstream end of the pore pressure line while maintaining 5 MPa at the upstream. We waited for steady-state flow, which was considered to be achieved when both a steady flow rate and steady internal pore pressure were observed. The downstream pore pressure was then reconnected to the intensifier, we waited again for pore pressure equilibration and resumed the loading process. A total of 23 flow-through tests were conducted this way from peak stress until residual stress was fully achieved. In addition to flow rate and pore pressure data, we use the intensifier volume record to track the rock's pore volume change throughout the experiment. The changes in intensifier volume are assumed to result from pore volume changes in the sample, except during the flow-through test. We therefore corrected the pore volume record for the volume loss during imposed flow. During deformation, a delay may exist between volume change in the rock and the intensifier. The true pore volume change is measured only at the end internal pore pressure equilibration phase just prior to a flow-through test.

2.4. Data Processing

The pore pressure transducer responses to changes in confining and fluid pressure were calibrated by imposing uniform, stable fluid pressures in the sample at a number of different confining pressures (for a detailed description of the calibration procedure, see Brantut and Aben (2021)). The variations in fluid pressure during the test were then computed by substracting the contribution of the known confining pressure in the pressure vessel. At a confining pressure of 85 MPa and a pore pressure of 5 MPa, we observed absolute accuracies of up to 0.06 MPa and standard deviations of up to 0.01 MPa for short-term measurements of the order of minutes. The calibration was conducted twice, prior to and after deformation (around 14 days apart). A long-term drift in the calibration factors (by around 5% between the first and second set) was observed, and we only used the second calibration, which was conducted immediately following the deformation test.

The continuous waveform data recorded at 10 MHz was processed to extract AE events. The data were first filtered with a second order Butterworth, 1 MHz low-pass filter. A first detection was conducted by extracting potential event windows where a threshold 80 mV amplitude was reached on more than 4 sensors within a time

interval 40 μs. The detection was confirmed by running an STA/LTA check, using a 2 μs short window and a 6 μs long window and a detection threshold of 20 dB on 5 channels. A total of 9,932 events could be detected this way. Among those, events associated to active surveys were identified by checking systematic waveform clipping of the source channel, and excluded from further analysis.

The active survey data separately acquired at 50 MHz with triggered digital oscilloscopes were processed to estimate the evolution in P wave speed and its anisotropy throughout the experiment. The method consists of (a) the manual picking of arrival times on an initial set of waveforms between each pair of transducers, yield absolute values for wave speeds, and (b) an automatic tracking of differences in arrival times by cross-correlation between the initial reference waveforms and subsequent waveforms on the same pairs of sensors (e.g., Brantut, 2015).

The wavespeed evolution was further processed by extracting, for each survey, a scalar anisotropy parameter α characterizing the ellipticity of the group wave speed with respect to the axis of compression, according to

$$V(\theta) = V_{\text{axial}}\left(\cos^2\theta + \alpha\sin^2\theta\right), \tag{1}$$

where V_{axial} is the wave speed along the compression axis, and θ is the group propagation angle measured from the compression axis. The empirical formulation Equation 1, with a constant V_{axial} and time-dependent α, was used as our velocity model in the AE location procedure.

P wave arrival times were picked on all waveforms of AE events using the method of Sleeman and van Eck (1999) (based on the Akaike information criterion), and a collapsing grid-search algorithm was used to locate the AE hypocenters. The method consists of systematically searching for the hypocenter location associated to the least absolute value of the difference between picked and computed arrival times. The 3D space is searched in a hierarchical way, by looking for the global minimum of the misfit on an iteratively finer and finer square grid, with step sizes of 5, 1 and 0.2 mm. The use of the least absolute value criterion makes the method robust to outliers in arrival time picks. The absolute accuracy of AE hypocenter locations is difficult to assess, since it largely relies on the prior knowledge of the velocity model. Using active surveys as events with known source locations, we estimate the accuracy to be of the order of 1–5 mm. We expect the accuracy to be the worst when the sample becomes very heterogeneous, that is, when our velocity model becomes very inaccurate. These problems can be mitigated by conducting a full AE tomography of the sample as in Aben et al. (2019), but this was not attempted here since the AE locations were only used to obtain a first order estimate of the rupture propagation front.

3. Results

3.1. Hydrostatic and Pre-Peak Data

Prior to deformation, we conducted a series of flow-through tests at increasing confining pressure, ranging from 10 to 85 MPa, using an upstream pore pressure of 5 MPa and a downstream pore pressure of 0 MPa (vented to the atmosphere). The steady-state flow rate decreases with increasing confining pressure (Figure 2a), which can be explained by a corresponding decrease in the sample's permeability. Under steady-state flow, the exact permeability value is expected to be given by Darcy's law,

$$k = C\frac{q}{A}\eta\frac{L}{p_{\text{up}} - p_{\text{down}}}, \tag{2}$$

where q is the flow rate, A is the sample's cross-sectional area, L is the distance between the tips of the two boreholes, and p_{up} and p_{down} are the upstream and downstream pore pressures, respectively. The factor C is a geometrical correction factor that accounts for the complex internal geometry of the flow path. In general, C depends on the presence of boreholes and notches, as well as on the presence of possible fractures that could focus the flow in certain regions of the sample. Here, we anticipate that internal flow geometry will evolve as the sample gets deformed (see next Section), so we simply recast the measured flow rate into an apparent permeability defined as

$$k_{\text{app}} = k/C. \tag{3}$$

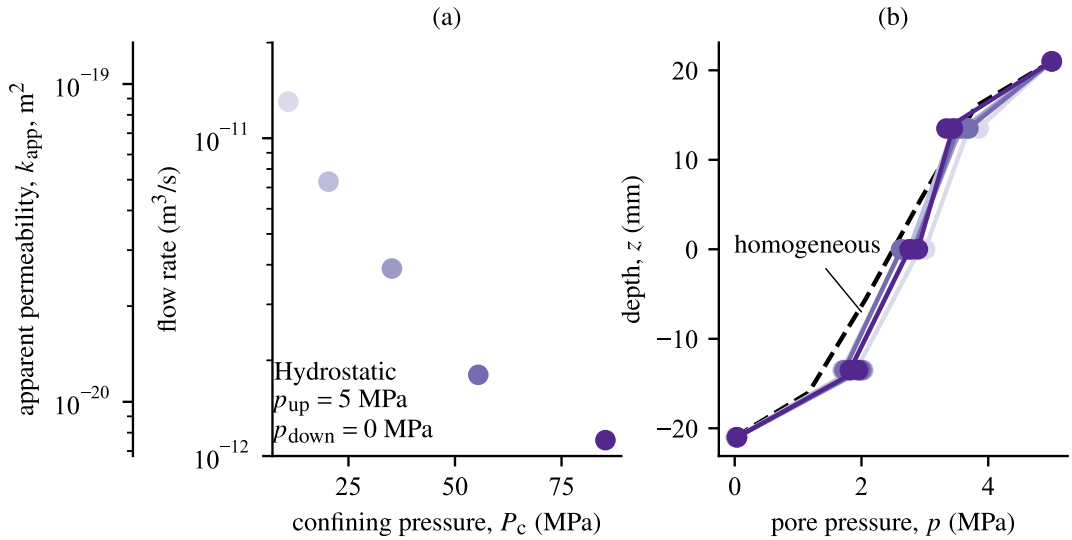

Figure 2. Transport properties of intact Westerly granite (sample WGMS2) under hydrostatic conditions. (a) Steady-state flow rate under a 5 MPa pore pressure gradient as a function of confining pressure. The apparent permeability k_{app} is computed using Equations 2 and 3. (b) Pore pressure value at each sensor location during steady flow under hydrostatic conditions, displayed here as a function of vertical position measured from the center of the sample. The symbols are colored according to the confining pressure, as displayed in panel (a). The dashed line correspond to the pore pressure distribution in a homogeneous sample.

Prior to deformation, we can consider that the sample is homogeneous. In that specific case, we can compute the C factor by comparing the flow rate computed in the true sample geometry, including boreholes and notches, to that obtained in a simple cylindrical geometry without any internal complexity (see Appendix A). We find that $C \approx 1.511$, that is, the apparent permeability underestimates the true one by about 1/3.

The internal pore pressure distribution during steady-state flow gives an indication of fluid flow heterogeneity in the sample. For homogeneous flow, we expect a constant pore pressure gradient between each pore pressure sensor. Deviations from such a reference pore pressure gradient can reveal areas with relatively higher or lower permeabilities. A reference pore pressure profile expected for homogeneous flow was obtained using a 3D flow model (see Appendix A) that computed the expected pore pressure at each sensor location, assuming a homogeneous matrix permeability (dashed line in Figure 2b). The higher pore pressure gradients between the two top sensors and two bottom sensors are due to the three dimensional nature of the flow around the borehole and notch regions. For the intact sample, the observed internal pore pressure distribution during steady-state flow indeed shows that the sample is close to being homogeneous (Figure 2b), as the comparison to our measured data shows only small differences near the downstream end of the sample. Our measurements also show that changes in confining pressure have no substantial effect on the pore pressure distribution.

With increasing differential stress, prior to peak strength, the apparent permeability initially remains stable, and then increases substantially above around 300 MPa (Figures 3a and 3b). After a maximum differential stress of around 400 MPa (lower than the failure stress of the rock) upon unloading, the permeability decreases gradually but remains roughly one order of magnitude greater than before loading. Internal pore pressure measurements during steady flow with a 5 MPa pore pressure difference show that the sample permeability becomes more heterogeneous with increasing load (Figure 3c). At the stage labeled "4," where differential stress was 400 MPa and prior to peak load, the pore pressure gradient decreases near the upstream end of the sample, indicating a local increase in permeability in this region. By contrast, at stage "5," where differential stress is the same (400 MPa) but along the unloading path, the pore pressure gradient is steeper than before in the upstream region, indicating a locally lower permeability in that part. This decrease in permeability is relative to the remainder of the sample volume: the permeability in stage "5" is on average larger than that in stage "4" (Figure 3b). After nearly complete unloading (stage "8"), the pore pressure gradient has decreased in both the upstream and downstream ends of the sample, which indicates locally higher permeability in these regions compared to a homogeneous sample.

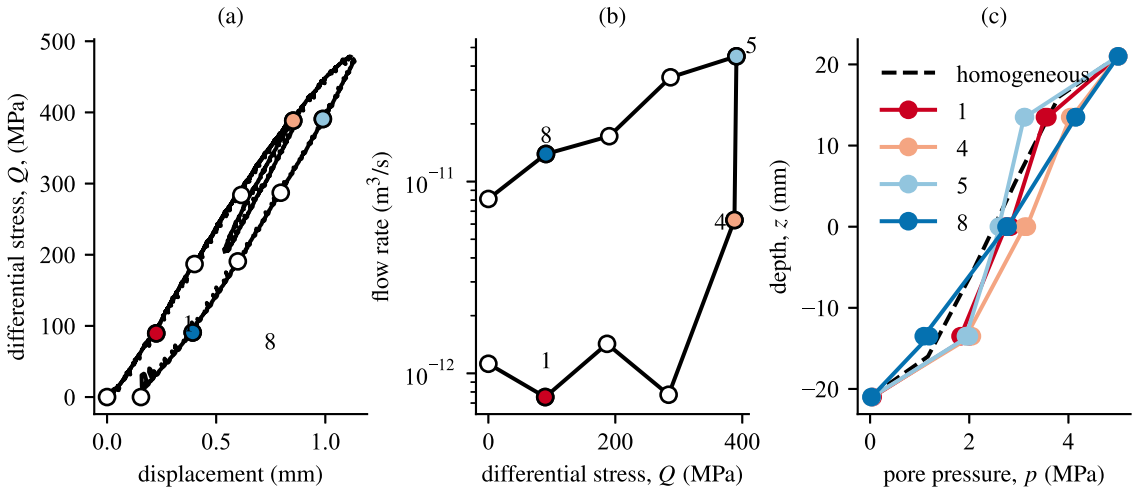

Figure 3. Transport properties of Westerly granite (sample WGMS2) during one load-unload cycle up to a maximum differential stress lower than the failure stress. (a) Stress-displacement curve. Each symbol corresponds to a stage when deformation was stopped, and constant flow rate was imposed across the sample using an upstream fluid pressure of 5 MPa and a vented downstream pressure. (b) Flow rate measured at each stage. (c) Pore pressure distribution during steady flow at stages 1, 4, 5 and 8, showed as a function of vertical position with respect to the center of the sample. The dashed line corresponds to a computation using homogeneous permeability.

3.2. Post-Peak Behavior

The deformation of the sample was conducted in a series of cycles so that the overall fracturing process was stable. The entire deformation process lasted around 102 hr, including periods where we imposed flow across the sample. With increasing axial displacement, differential stress initially increased, reached a peak (of around 475 MPa), and then drop abruptly down to a nearly constant residual strength of the order of 200 MPa (Figure 4).

The stress-displacement data can be recast into shear stress on the fault plane and fault slip, using methods described in Aben and Brantut (2023) which include strength corrections for the notch inserts and change in fault area. We report slip as "equivalent fault slip," which is the average inelastic displacement projected along the slip direction, referenced to the displacement at peak stress. In practice, as illustrated by the acoustic emission analysis (see below), the fault is not through-going at all times during the experiment, so our "equivalent fault slip" is only equal to the actual slip once the fault is complete.

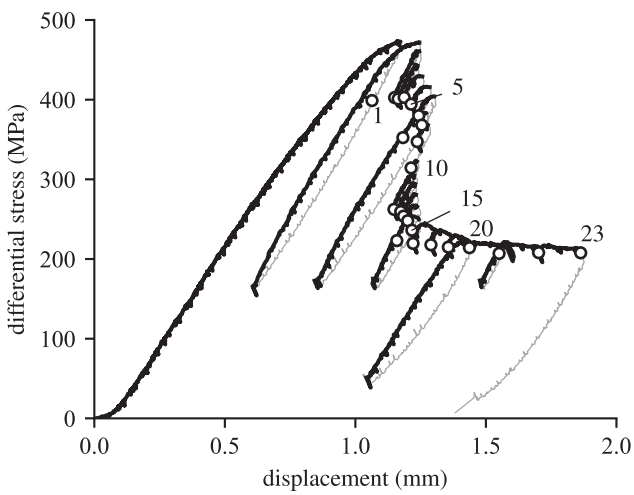

Figure 4. Differential stress as a function of axial displacement (sample WMSG4). Black lines correspond to loading, and thin gray lines correspond to unloading. Symbols mark stages when deformation was paused and constant flow rate was imposed across the sample.

The shear stress peaked at 250 MPa, followed by a decrease with ongoing slip down to a residual value of around 100 MPa. The slip-weakening distance was of the order of 0.5 mm (Figure 5a). The flow rate measured across the sample during flow-through stages increased dramatically prior to peak stress, from 2×10^{-12} m^3/s before deformation to 1.2×10^{-10} m^3/s at peak stress: a two orders of magnitude rise. The pre-peak increase observed in sample WGMS2 (Figures 3b and 5b, gray line) was consistent with that observed in sample WGMS4. Subsequently, the flow rate underwent a gradual increase with increasing deformation, up to 3.6×10^{-10} m^3/s at 1.5 mm slip, which amounted to a factor of three increase compared to the flow rate at peak stress. In terms of apparent permeability, the increase from intact to peak stress was from around 10^{-20} m^2 to 7.5×10^{-19} m^2, with a final k_{app} of around 2.3×10^{-18} m^2 at 1.5 mm slip.

For all experiments, including those where fluid flow was restricted at the borehole due to blockage, we also recorded the pore fluid volume change in the intensifier when pore pressure was equilibrated throughout the sample. This procedure allowed us to monitor the evolution of pore volume throughout the experiments (Figure 5c). At the onset of loading, the pore volume decreased by around 0.06 to 0.09 cm^3. This decrease occurred at near

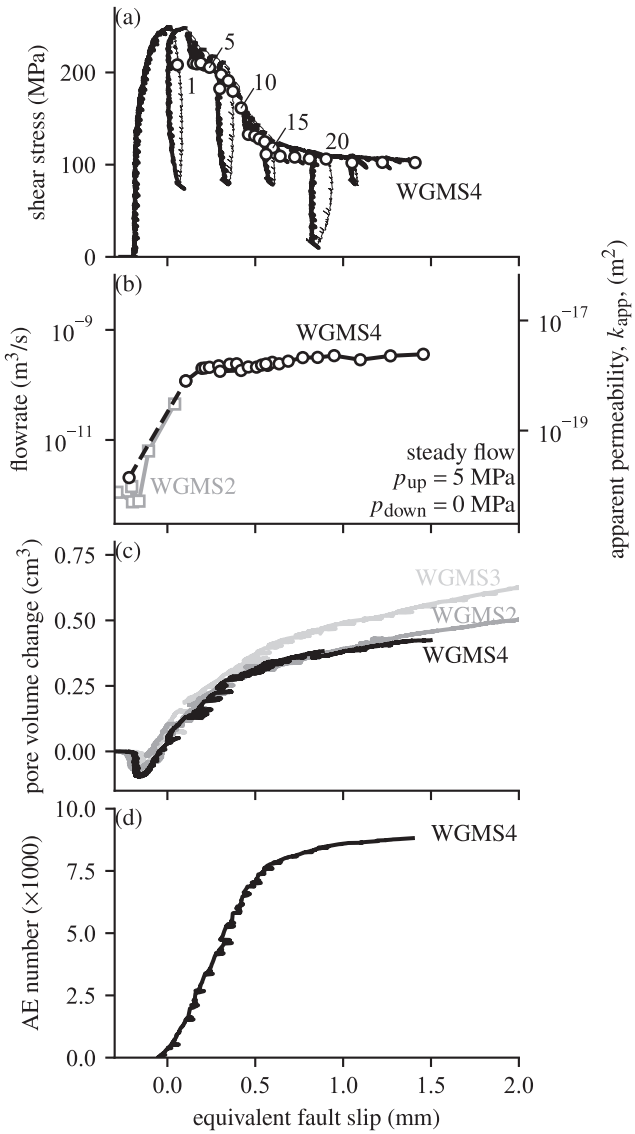

Figure 5. (a) Shear stress, (b) flow rate, (c) pore volume change and (d) cumulative AE number as a function of equivalent fault slip. Black lines correspond to sample WGMS4, which could be deformed without borehole blockage.

zero equivalent slip, that is, it occurred during the purely elastic loading phase. The pore volume then reached a minimum, and increased linearly with increasing equivalent slip (i.e., with increasing inelastic axial strain) up to peak stress and until around 0.4 mm slip, just before shear stress dropped below 200 MPa. The increase in that phase was of the order of 0.3 cm^3. Then, with ongoing slip, the pore volume kept increasing at a smaller rate, of the order of +0.14 cm^3 over 1.1 mm slip. The pore volume data show that the net effect of fracture and slip was dilatant, with a dilatancy rate that was stronger prior to failure than after failure.

The cumulative number of AEs increased linearly with increasing slip up to around 0.57 mm slip, where the total number of AEs was around 7,500. Beyond that point, AE activity decreased and the cumulative number of events only increased by around 1,200 from 0.57 to 1.5 mm slip (Figure 5d).

During the initial loading stage up to the peak stress (before stage 1, Figure 4), AEs were clustered in linear, subvertical regions emanating from the notches (Figure 6). These regions continued to grow with increasing deformation. At stage 2, the bottom cluster extended on the western side and reached the middle of the sample while the top cluster remained confined to the upper 1/4 of the sample. At stage 3, the upper cluster propagated downwards, mostly on the Eastern side of the sample. The top cluster kept propagating downwards during stage 4 and 5, and the active region deviated from the vertical and approached an angle of 30° with respect to the compression axis. In stages 6–8, the bottom cluster propagated upwards and progressively oriented itself at 30° from the vertical. It is only at stage 9 and onwards that the two clusters became connected and aligned at 30°. At stages 10 and 11, AE activity was clustered on the western side of the sample, which appeared to be the last "unbroken" region left along the 30° orientation. Stages 10 and 11 also coincide with a dramatic decrease in the shear stress supported by the sample (Figures 4 and 5a). In stage 12 and 13, AE activity was clustered in the upper part of the sample, on both sides. From stage 14, AE activity was distributed along a narrow region oriented at 30° from the compression axis.

Overall, AE locations show that the rupture process initiated with the growth of fracture zones emanating from the preexisting notches, and that these fracture zones became fully connected to form a complete fault only at stages 10–11, when the sample experienced its final weakening phase. The propagation of the shear rupture was not uniform across the strike and dip of the fault, and the upstream region seemed to have ruptured last from West to East.

The measurements of pore pressure at different locations along the sample allow us to observe in more detail the relationship between local permeability evolution and the spatio-temporal evolution of the fracturing process imaged by AEs. For each flow-through stage, we measured the pore pressure distribution $(p_1, \ldots, p_4)$ on the western side of the sample, and $(p_5, \ldots, p_8)$ on the eastern side (Figure 1c), and compared these measurements to the predictions in a homogeneous material (Figure 7). At peak stress (stage 1), the pore pressure distribution was only slightly different from the homogeneous reference: p_7 was slightly below the reference, which indicates a slightly lower permeability in the central, eastern part of the sample. Similarly, the local pressure gradient between p_2 and p_3 was larger than the reference, also indicating that the central region was less permeable than the upstream and downstream regions. During the next increments of slip, from stage 2 up to stage 10, we observed a marked drop in p_5, p_6 and p_7 (eastern side), as well as in p_2, p_3 and p_4 (western side), compared to the reference. These drops indicate that the upstream region of the sample, on both sides, had a lower permeability than the downstream region. The local pressure gradient between p_{up} and p_5 was around twice larger than anticipated in a homogeneous sample, which tends to indicate that the local permeability in the upstream part was approximately twice smaller than the average. The heterogeneity in pore pressure distribution remained stable until stage 10, beyond which we observe

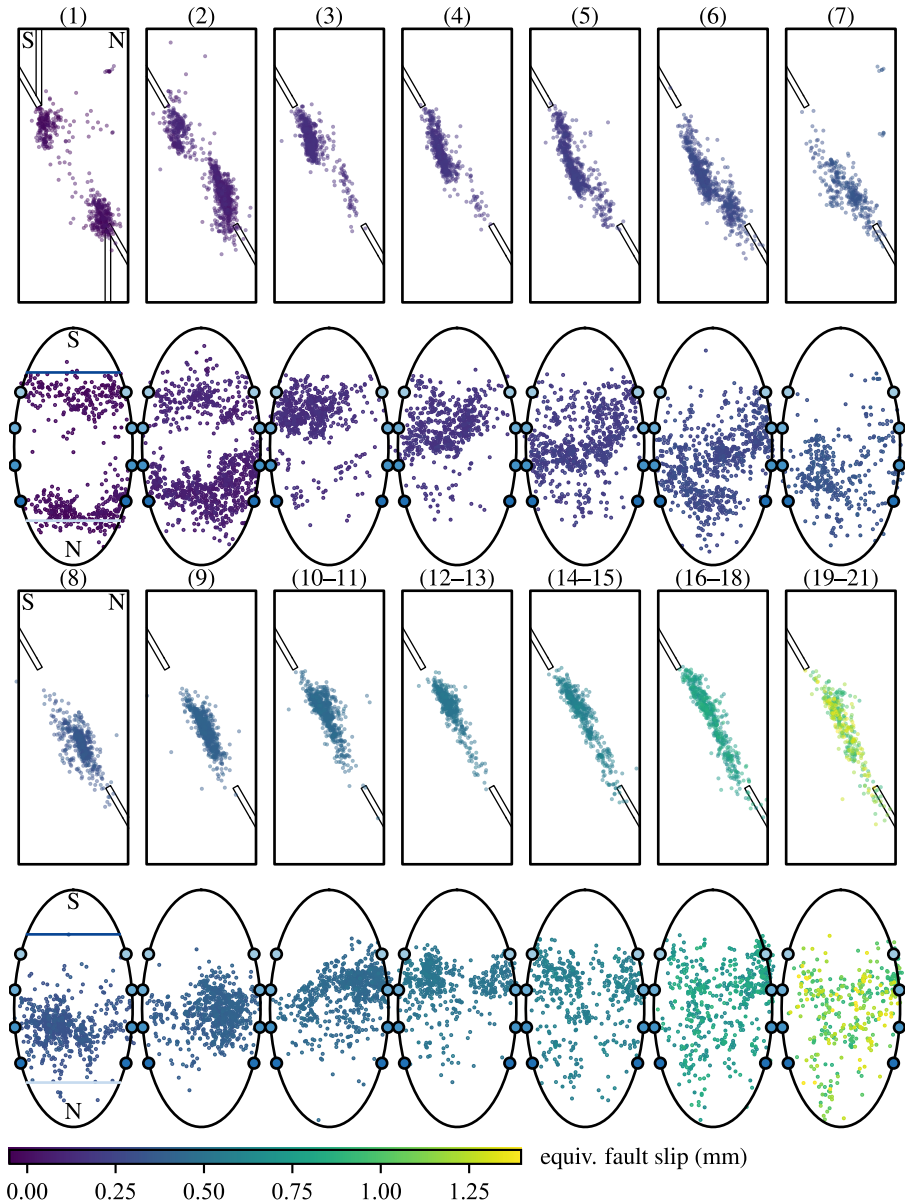

Figure 6. Sequence of AE locations obtained between each flow-through stage. Stage numbers are shown in parentheses—these numbers correspond to those labeled in Figures 4 and 7. The top row shows the locations in the North-Depth plane (North and South are indicated at the top of the first plot), and the bottom row shows the same locations projected on the fault plane (North and South are also indicated in the first plot). Blue circles at the edge of the fault plane indicate the positions of pore pressure sensors, from upstream (dark blue) to downstream (light blue). The dark and light blue lines show the limits of the upstream and downstream notches, respectively. All AE locations are colored according to the equivalent fault slip at which they occurred (see colourbar).

a gradual return (from stage 11–15) to a distribution consistent with a homogeneous permeability along the fault. Beyond stage 15, the pore pressure distribution did not change further, except for p_4 which drifts toward lower values. This drift was substantial, and difficult to interpret: it could imply a locally large permeability between the sensor located at p_4 and the notch, combined with a much smaller permeability between p_3 and p_4. Assuming no unusual measurement error, this change in permeability would be very local, since it only impacts the western side, downstream end of the sample.

In the entire post-failure region, stress gradually dropped and the flow rate measured during flow-through stages increased with increasing slip. There was an exception to this steady increase (Figure 7): between stages 7 and 8,

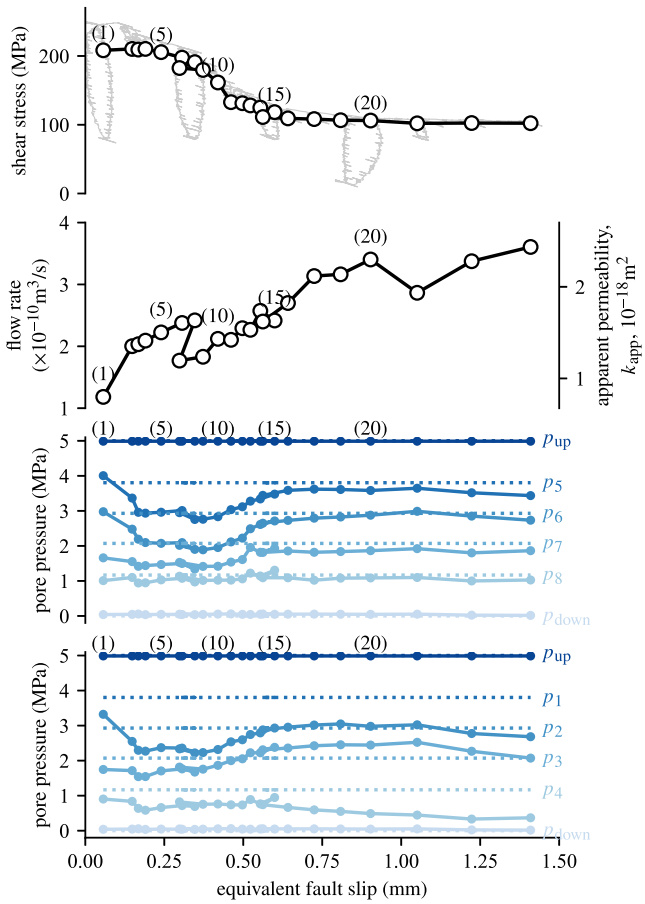

Figure 7. Detailed evolution of shear stress, flow rate, and pore pressure profiles as a function of equivalent fault slip. Pore pressure profiles during constant flow rate are shown for each flow-through stage, including upstream (5 MPa) and downstream (0 MPa) pore pressures. The sensor measuring p_1 experienced large drift throughout the experiment, and the data are thus not reported. Dashed lines correspond to the expected pore pressure at each position in the case of a homogeneous rock (including the presence of notches and boreholes). Deviations from the dashed lines indicate heterogeneous flow and permeability structure; pore pressures lower than those in the homogeneous scenario indicate a low permeability upstream relative to other parts of the sample.

the shear stress was dropped below 100 MPa, and we waited overnight before resuming the experiment. Upon reloading to the same stress, we observed that the flow rate was lower than before unloading, by around a factor 0.7. The value of equivalent slip was also slightly below that at the previous stage, indicating net backslip associated to the unloading operation. A similar observation was made between stages 20 and 21: upon reloading, the flow rate was measurably smaller than prior to unloading, by a factor 0.8.

3.3. Decompression

After deformation and unloading, confining pressure was decreased in several steps at which we conducted flow-through tests (Figure 8). We observed an increase in average flow rate (and thus apparent permeability) with decreasing confining pressure, with flow rate changing from 3.7×10^{-10} cm^3/s at $P_c = 85$ MPa, up to 6.4×10^{-9} cm^3/s at $P_c = 10$ MPa (Figure 8a). The pore pressure distribution at $P_c = 85$ MPa showed a larger than average gradient at the downstream end of the sample, indicating a locally lower permeability in that region (Figure 8b). With decreasing confining pressure, the pore pressure gradient became increasingly larger in the lower half of the sample, indicating that the permeability became more heterogeneous, with an upper region of the sample being more permeable than the lower half.

3.4. Fault Zone Structure

The deformed sample shows a clear shear fault zone extending from both notches (Figure 9). The fault zone is around 5–10 mm in width, and is formed by several thin fractures. On the eastern side, the fault zone is relatively narrow (up to 5 mm width) and the fractures are mostly oriented at 30° from vertical. On the western side, the fault zone is wider (up to 10 mm width). Two main fractures emanate from each notch, and they initiate at angles steeper than 30° from vertical. The fracture extending from the upstream notch terminates in the rock and does not appear connected to the rest of the fault zone. The fracture extending from the downstream notch forms the main shear plane and is connected to the upstream notch via a heavily damaged region spanning the upper part of the fault (between sensors 5 and 6).

X-ray computed tomography (CT) sections of the deformed sample (Figure 10) reveal that a clear main fracture connects the notches. On the eastern side, this main fracture is straight, oriented at 30° from the compression axis. On the central part and western side, the main fracture is more curved but remains clearly continuous. In addition, we observe steep, subvertical wing cracks emanating from both notches. Some of these cracks terminate within the rock matrix and are not connected to the main fracture. Superimposed on those key features, we also observe a number of horizontal fractures, which can be attributed to decompression effects. Overall, the internal fault structure obtained from the CT scans (at the CT resolution of 28 μm voxel size) is consistent with surface observations, and even appears somewhat simpler than anticipated from the surface traces. The curved wing cracks seen on the western side of the sample are clearly present internally, but they appear much narrower than the main fracture connecting the notches. Of course, the CT observations were made after complete decompression, and the actual aperture of each fracture was likely much narrower at elevated applied stress.

4. Discussion

4.1. Summary of Key Observations

Our experimental data show that the overall permeability of Westerly granite increases dramatically with increasing applied stress, up to the peak stress and the onset of fault propagation. This increase, on average, is of

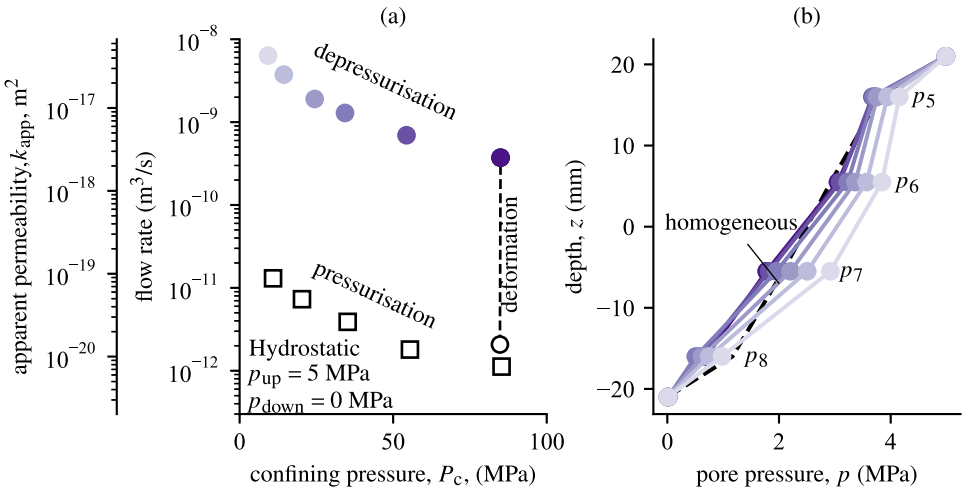

Figure 8. Transport properties of intact (WGMS2, squares) and fractured (WGMS4, circles) as a function of confining pressure. (a) Steady-state flow rate under a 5 MPa pore pressure gradient as a function of confining pressure. The apparent permeability k_{app} is computed using Equations 2 and 3. (b) Pore pressure value at each sensor location ($p_5, \ldots, p_8$, Western side of the sample) during steady flow under hydrostatic conditions, displayed here as a function of vertical position measured from the center of the sample. The symbols are colored according to the confining pressure, as displayed in panel (a). The dashed line corresponds to the pore pressure distribution in a homogeneous sample.

around two orders of magnitude, from around 10^{-20} m^2 to 10^{-18} m^2, which is consistent with previous data sets obtained during cycling loading up to peak stress (Mitchell & Faulkner, 2008; Zoback & Byerlee, 1975) and beyond (Kluge et al., 2021).

Strikingly, the average permeability increases only moderately from peak stress onwards, as the shear fault initiates (from both notches) and propagates across the entire sample. The increase in apparent, average permeability is of around a factor 3 at 1.5 mm slip. This increase is consistent with similar measurements during shear fracture of granite (Kluge et al., 2021).

Our data are somewhat different from the post-peak permeability measurements of Kiyama et al. (1996), which were conducted in granite at much lower confining pressure (5 MPa). Their results show only one order of magnitude increase permeability in the rock up to peak stress, and another two or more orders of magnitude increase with ongoing deformation beyond peak stress. These differences can be attributed to the low confining pressure employed by Kiyama et al. (1996), which brings the sample in nearly uniaxial conditions. The geometry of the fault formed in their experiment was not reported, but they report dramatic increases in lateral strain in the post-peak region, which is consistent with fault zone opening and possibly axial splitting. We conclude that the permeability evolution during deformation of granite is strongly influenced by confining pressure and faulting style.

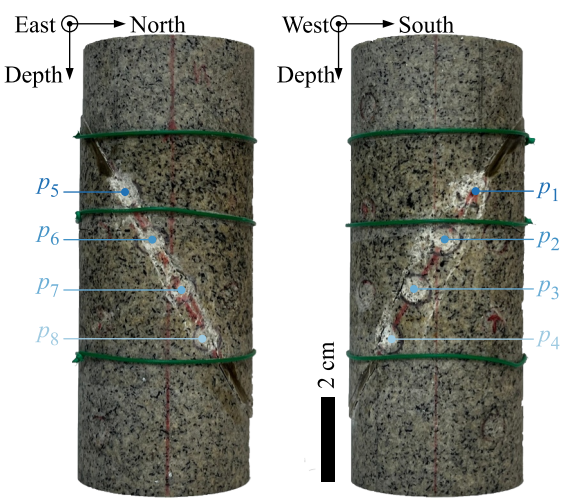

Figure 9. Photographs of the deformed sample (WGMS4).

The permeability difference after unloading of an undeformed sample and that of a deformed sample with a shear fracture suggest that the shear fracture is the primary fluid pathway in the deformed sample. The internal pore pressure measurements during steady flow indicate the development of local permeability heterogeneities, which we suggest arise from the development of the through-going shear fracture that was imaged by AE locations and, after deformation, by CT scans. The apparent bulk permeability's presented above are thus a composite of fault zone permeability and host rock permeability once the fault starts forming at the peak stress. The relative contributions of, and change in, bulk and fault zone permeability's will evolve with fault formation. For instance, a notable feature is that the upstream end of the sample seems to retain a lower permeability than average until the fault becomes through-going. The AE locations, surface observations and CT scans

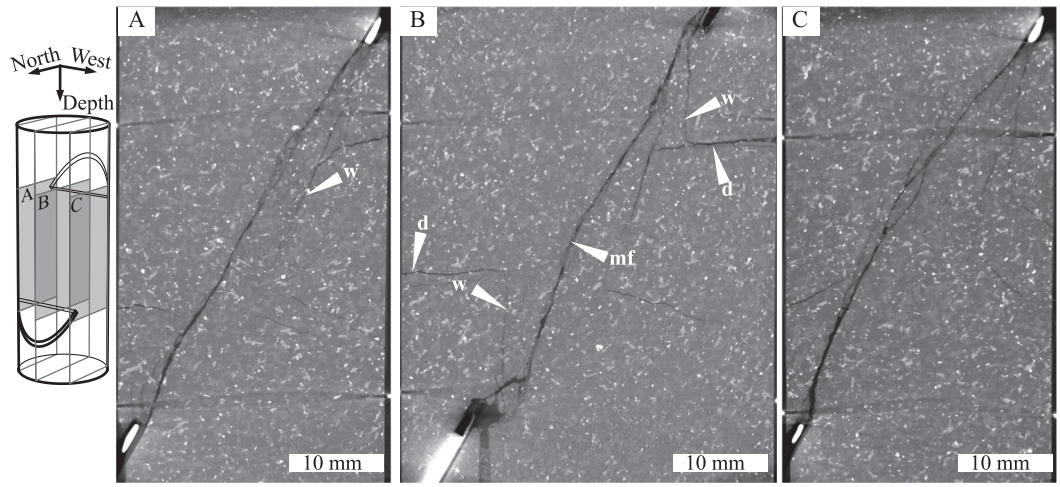

Figure 10. X-ray micro-CT sections of the deformed sample (WGMS4). Scans were obtained using a Nikon XTH225 X-Ray CT scanner. Images were reconstructed from 3,185 projections, with an exposure time of 0.5 s each, and an x-ray source operating at 200 keV and 104 μA. Voxel size is 28 μm. w: wing cracks. d: decompression cracks. mf: main fracture.

all indicate the early development of wing fractures emanating from the notches, but these are not necessarily connected to the main fault. It is only when the upper region becomes properly fractured along the main fracture plane (as imaged by the AE locations during stages 10 → 13) that the upstream end of the sample becomes as permeable as the rest of the fault.

4.2. Evolution of Hydraulic Transmissivity During Faulting

Up to this point we have used the data from our flow-through tests to quantify the average apparent permeability, and used the internal pore pressure data to make qualitative estimates of permeability heterogeneity. We can make more quantitative estimates by assuming that the fault zone is consistently more permeable than the bulk, so that we can consider that fluid flow occurs mostly along the fault, and use our local pore pressure data to estimate local hydraulic transmissivity along the fault dip. Although this assumption may be somewhat incorrect at early stages of the experiments, when the fault has just initiated and fluid flow is expected to be truly three-dimensional, we expect it to be a good approximation of the flow geometry when the fault extends over a large fraction of the sample, and when the differential stress is decreasing. Indeed, the permeability of the off-fault material is expected to decrease upon unloading (e.g., Mitchell & Faulkner, 2008; Zoback & Byerlee, 1975), further amplifying the difference between on- and off-fault permeability.

In general, fluid velocity **u** is related to pressure gradient following Darcy's law:

$$\mathbf{u} = -\frac{\mathbf{k}}{\eta}\nabla p, \tag{4}$$

where **k** is the permeability tensor, η is the fluid viscosity, and ∇p is pore pressure gradient. The geometry of our sample was chosen to maximize flow along the prospective fault zone, so that the largest pore pressure gradient is along the fault zone dip direction. In that situation, under steady flow conditions, the fluid flux q is given by

$$q = \ell(x)t(x) \times \frac{k_f(x)}{\eta}\frac{dp}{dx}, \tag{5}$$

where ℓ is the lateral extent of the fault, t is the fault thickness, and k_f if the fault permeability. All these quantities should depend on position x along the fault. Equation 5 is a strong simplification that neglects fluid flow in the bulk. Thus, the fault zone thickness t and permeability k_f should be considered together as the effective hydraulic transmissivity of the fault zone, $k_f t$. At all flow-through stages of the experiment, we can compute the local

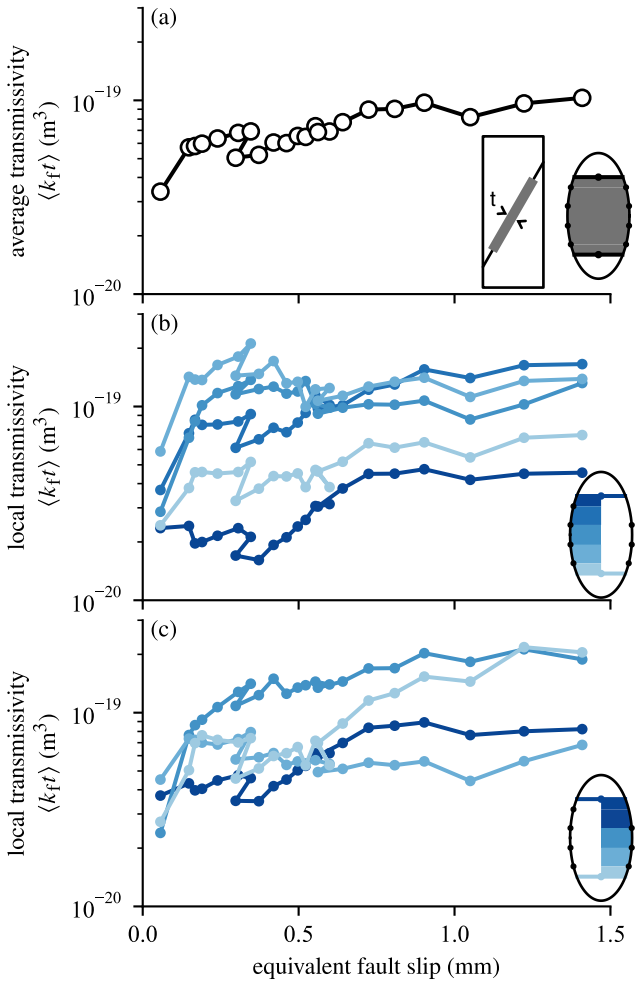

Figure 11. Average and local apparent fault zone transmissivity as a function of equivalent fault slip. See Equation 6. (a) Average fault transmissivity $\langle k_f t \rangle$. (b) Local apparent transmissivity for the Western side of the fault, assuming uniform flow. Colors range from dark blue (upstream) to light blue (downstream end), as depicted in the sketch. (c) Same as (b) for the Eastern side of the fault. Due to sensors malfunction, pressure p_1 could not be measured an only the average estimated transmissivity is reported for the two upstream regions (dark blue).

average along-fault pore pressure gradient between pairs of transducers, and determine the average transmissivity $\langle k_f t \rangle$ for each subregion of the fault:

$$q = \langle \ell \rangle_i \frac{\langle k_f t \rangle_i}{\eta} \frac{\Delta p_i}{\Delta X_i}, \tag{6}$$

where $\langle \ell \rangle_i$ is the average lateral extent of the fault in region i, $\langle k_f t \rangle_i$ is the average, apparent transmissivity in that region, Δp_i is the pore pressure drop across region i, and ΔX_i is the size of the region (i.e., the distance down-dip between pairs of transducers). Since local flow rates are not measured, we assume a homogeneous flow rate across the sample. This, and the 1D flow assumptions, lead to the estimates being approximations. These estimations should be interpreted as lower bounds for the permeability (or transmissivity) changes: If we infer a locally higher permeability in a given region from the pressure drop heterogeneity during flow, then the local flow rate consistent with that larger permeability could be larger than the homogeneous one assumed here. Thus, the actual permeability should be larger than that inferred with our simple method. Of course, 3D flow effects make such statements hard to generalize with absolute certainty, especially if flow is not dominantly parallel to the fault. We will therefore call the transmissivity estimates "apparent," pending a more complete three dimensional flow analysis.

The average transmissivity of the entire fault increases with increasing equivalent fault slip, from around 3×10^{-20} m^3 at peak stress up to 10^{-19} m^3 after 1.5 mm slip (Figure 11a). This range of values is similar to that measured in saw-cut fractures in Westerly granite at elevated pressure and applied shear stress (Rutter & Mecklenburgh, 2018).

The local transmissivities are roughly similar throughout the sample at the onset of slip (Figures 11b and 11c), with a range from 2×10^{-20} m^3 to 6×10^{-20} m^3, indicating a relatively homogeneous sample at peak stress. With ongoing equivalent slip up to 0.45 mm, the transmissivity in the fault zone becomes more heterogeneous: All transmissivities increase by about a factor to 3, except that estimated in the upstream end of the sample. From 0.45 to 0.7 mm (stages 10–13), the transmissivity in the upstream region increases by around a factor 2. A slight increase in transmissivity is also observed in the region directly downdip of the upstream one. Another interesting feature is that the transmissivity in the centermost region of the fault slightly decreases during that phase, by around a factor 2. The completion of the shear fracturing process, with the fault zone being fully connected across the sample, is thus marked by a relative homogenization of the hydraulic transmissivity, together with the main shear stress drop down to a stable residual frictional strength (Figure 5). With ongoing slip beyond 0.7 mm, local transmissivities remain mostly stable.

The heterogeneity in transmissivity during the main shear stress drop is correlated the fracturing process as highlighted by the AE locations (Figure 6). There is a general trend of increasing transmissivity at the onset of AE activity, as shown by cumulative AE density in the ±10 mm thick fault zone (Figure 12). However, on the local scale the picture is more complex: For example, AE activity at the upstream end is located mainly along a wing crack emanating from the notch, which is not connected to the main fault zone (Figure 6, stage 2 and 3). Therefore, the transmissivity remains low here whilst it increases in other regions. During stages 10–13, the fault zone becomes fully connected, as seen by the AE activity in the upstream part of the fault. The upstream transmissivity also increases in that region (Figure 6, stages 10–13), but there is no clear quantitative correlation between the local AE density and transmissivity (Figure 12, dark blue curves).

A similar increase in transmissivity concurrent with low AE density is seen for the downstream regions, especially on the eastern side (Figure 12b, pale blue curve). At the onset of fault slip, AE activity here is high (Figure 6,

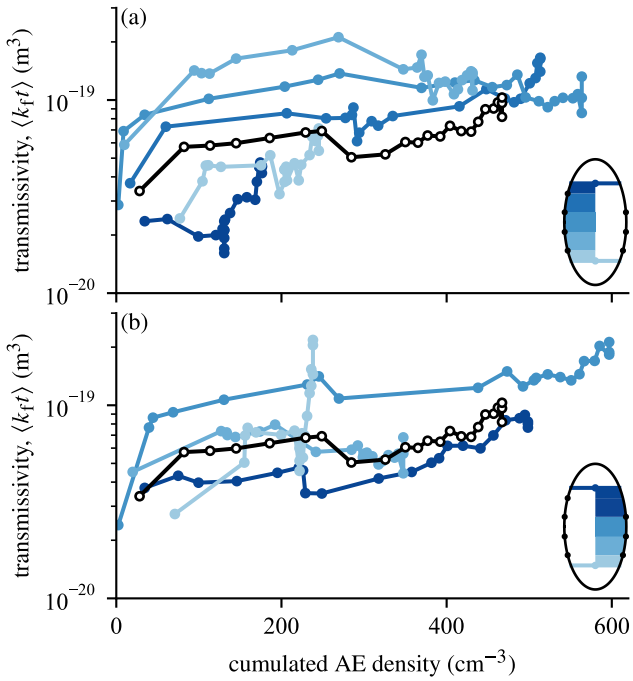

Figure 12. Average and local apparent fault zone transmissivity as a function of cumulative AE density. (a) Average (black curve) and local apparent transmissivity for the Western side of the fault, assuming uniform flow. Colors range from dark blue (upstream) to light blue (downstream end), as depicted in the sketch. (b) Same as (a) for the Eastern side of the fault. Due to sensors malfunction, pressure p_1 could not be measured an only the average estimated transmissivity is reported for the two upstream regions (dark blue). AE densities were obtained from AEs located in a ±10 mm wide band around the 30° fault trajectory.

stage 2) and transmissivity shows an initial increase. A second increase starting at stage 8 and 9 is coincidental with heightened AE activity at the region just near it. The initial increase suggests some degree of connection of this region with the notch and the main fault zone. The second increase in transmissivity may be caused by further development of the fracture in the adjacent area, although we observe a slight concurrent drop in transmissivity in there (Figure 12b). An additional factor is the heterogeneous stress field during shear fracture formation, which may cause temporary closure of the downstream section until the fracture matured further. Thus, AE locations and density do not provide a 1-to-1 correlation with transmissivity increase, but may shed light on a complex process of shear fracture formation and linkage.

After the main shear stress drop, at slip beyond 0.7 mm, transmissivity is mostly stable, despite a net increase in pore volume that indicates continued dilation (Figure 5). Our results on freshly fractured granite are qualitatively different from observations on saw-cut fractures or artificial quartz-rich fault gouges: in those cases, transmissivity (or permeability) is always shown to decrease substantially with increasing slip (e.g., Crawford et al., 2008; Rutter & Mecklenburgh, 2018; Zhang et al., 1999), and is associated with compaction. This behavior can be attributed to the fact that the initial state of saw-cuts and artificial fault gouges is "unconsolidated," that is, well above "critical state" (e.g. Muir Wood, 1990, chap. 6): any shear strain increment produces compaction by asperity crushing and grain rearrangements, which severely decreases fluid transport capabilities. By contrast, initially intact rocks should be viewed as "overconsolidated," well below critical state: shear strain increments produce net dilation, which initially increases transport properties. Our experiments reveal that only limited shear strains are required to achieve a plateau in permeability. Furthermore, we observe a change in regime from an initial phase, before peak stress, where dilation is large and permeability enhancement depends exponentially on dilation, to a post-failure phase where dilation is limited, and fault zone transmissivity is more or less stable or slightly increasing (Figures 5b and 5c). Between these two phases, that is, between peak stress and residual stress, the fault zone is forming by the creation and connection of branches, and the overall transmissivity is locally heterogeneous.

The local transmissivity estimates, together with AE locations, reveal the complexity of the fault zone formation process, and the key importance of fault branch connectivity. The completion of the fault across the sample marks a relative homogenization of hydraulic transmissivity. Even though some heterogeneities seem to persist (all within a factor of up to four of each other), our analysis is probably too approximate to firmly conclude on that point.

4.3. Pressure Sensitivity of the Fault

One additional feature that can be extracted from our data is the evolution of the pressure sensitivity of the rock hydraulic transport properties between the intact and fully fractured states (Figure 13). Both data sets follow a clear power law trend

$$\langle k \rangle \text{ or } \langle k_f t \rangle \propto P_c^n \tag{7}$$

with exponent n between −1.22 and −1.28. The pressure dependency is thus very similar between the intact rock and the shear fracture after 1.5 mm slip, which points to a potentially similar crack closure/opening mechanisms for the two samples, despite their large difference in microstructure.

The pressure dependency of fault transmissivity seems to follow a power law to a great degree of confidence. By contrast, an attempt to represent the transmissivity in terms of $\langle k_f t \rangle^{1/3}$ as a function of $\ln P_c$ shows a less clear

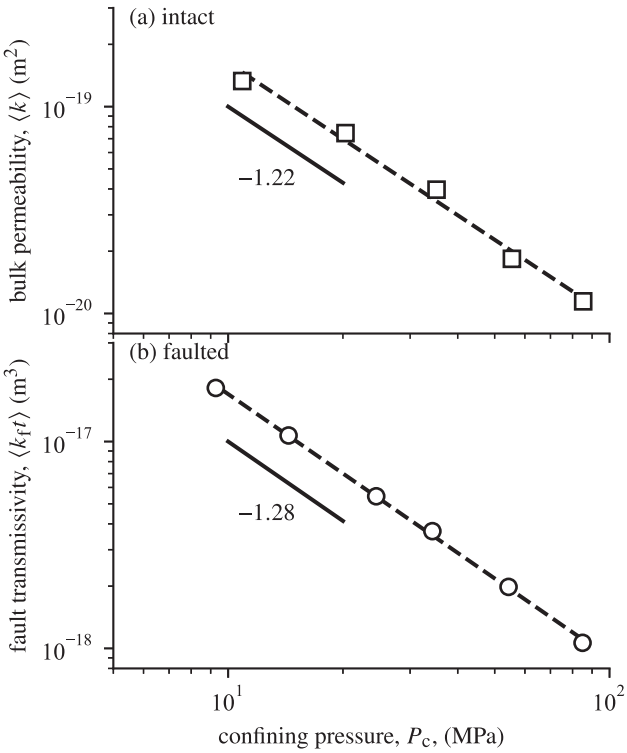

Figure 13. (a) Permeability of the intact rock (sample WGMS2) and (b) average hydraulic transmissivity of the fault zone (sample WGMS4) as functions of confining pressure. During each measurement, we used $p_{up} = 5$ MPa and $p_{down} = 0$ MPa. Permeability was computed assuming a homogeneous material, that is, including the appropriate correction factor (Equation 2).

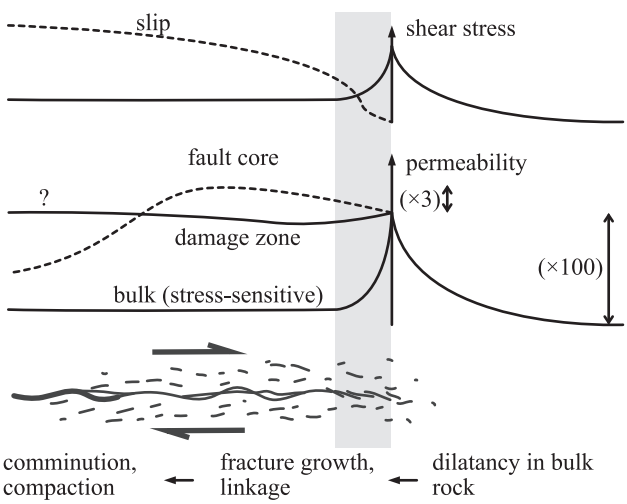

Figure 14. Synoptic, qualitative view of the evolution in permeability in a propagating shear rupture in a tight rock (intact rock or healed/sealed fault). Factors in parentheses are approximate increases measured in experiments conducted in Westerly granite or equivalent.

linear trend, as opposed to expectations and previous data sets on rough fractures with limited displacement (e.g., Walsh, 1981). Thus, the fault zone generated in the experiment is probably better viewed as a volume where permeability is enhanced, rather than a single fracture. This view is supported by the CT scans, which show clearly that the fault zone is formed by a set of connected fractures in addition to a principal slightly curved fracture. Furthermore, we expect this principal fracture to be filled with gouge particles generated by the fracturing process, and to be partially closed by the application of confining pressure.

4.4. Synoptic View of Hydraulic Transport Properties During Shear Rupture

We can combine our observations and attempt to draw some general conclusions about the evolution of permeability and fault transmissivity during the propagation of shear ruptures in "overconsolidated" (intact, sealed or healed) faults (Figure 14). In the following, we consider the sequence of processes along a propagating quasistatic shear rupture. We note that our results have been attained at stresses and strains somewhat below the peak stress and post-peak stress path for quasi-static rupture, as it is technically not possible to perform a steady flow-through experiment during ongoing fault growth. Nonetheless, we assume that the observed trend is similar to that at the post-peak stress path.

From a purely mechanical point of view, the shear stress ahead of the rupture tip region increases with increasing proximity to the tip (typically following an inverse squareroot trend if we assume linear elastic behavior of the intact rock). The "rupture tip" itself is a poorly defined concept in cohesive shear cracks, but for the purpose of our discussion we can consider a convention where the "tip" is defined as the location of the peak shear stress achieved on the fault. Beyond this location, stress degrades as net slip is accumulated across the fault, until residual friction is achieved. The region where this strength degradation occurs can be defined as the "cohesive zone" (shaded area in Figure 14), and corresponds to the growth and progressive linkage of shear and tensile cracks. Beyond the cohesive zone, strength is relatively stable (as observed in our experiments, and others in the literature (Lockner et al., 1991; Ohnaka & Shen, 1999; Wong, 1982)). Under dynamic conditions (with varying slip rates along the fault), weakening may spread further into the interior of the rupturing patch (e.g., Brantut, 2021; Brener & Bouchbinder, 2021; Paglialunga et al., 2022; Rice, 2006; Viesca & Garagash, 2015), but such effects are not considered here.

The striking feature of faulting in low porosity rock like granite is that most of the permeability increase occurs in the bulk prior to peak stress, that is, before macroscopic strain localization and peak stress. This increase in permeability can be attributed to the opening of existing microcracks due to increased shear stress, as well as the growth of new microcracks: this is the classical dilatancy effect (e.g., Brace & Byerlee, 1966; Tapponnier & Brace, 1976, among many others). As stress increases, microcracks concentrate and start to form a damaged process zone ahead of the main fracture plane (e.g., Moore & Lockner, 1995; Zang et al., 2000). When peak stress is achieved (at the rupture "tip"), strain localization initiates and we have to decouple the permeability of what can be termed the "fault core" and its surrounding damage zone, and beyond, the host rock. Our data show that the fault core permeability initially increases moderately with ongoing slip. Concomitantly, the host rock permeability is expected to decrease as shear stress is relaxed

(Mitchell & Faulkner, 2008; Zoback & Byerlee, 1975): cracks should close in the regions away from the main fault zone. The damage zone surrounding the fault core is a loosely defined concept at the scale of our experiments: it is typically a cm-wide region where microcrack density is larger (e.g., Aben & Brantut, 2021; Aben et al., 2019; Moore & Lockner, 1995; Zang et al., 2000), but our permeability measurements do not have the resolution to access the specific properties of that region. We anticipate that the very close proximity of the principal fracture, which is rough at multiple scales (e.g., Kluge et al., 2021), will generate a complex stress field (e.g., Chester & Chester, 2000) and maintain the opening of microcracks. Thus, we could hypothesize that the permeability of the damage zone remains relatively high, at an intermediate level between the principal fracture and the host rock. Finally, with further slip on the newly formed fault, we expect that fault core dilatancy saturates. The large shear strain within the fault core should lead to severe grain size reduction and wear of asperities (e.g., Boneh et al., 2014; Faulkner et al., 2018; Wang & Scholz, 1994), which should eventually lead to compaction and/or a decrease in fault core permeability, as observed in large strain gouges (Zhang et al., 1999).

The synoptic view presented above is consistent with that presented in Mitchell and Faulkner (2008). Our new data bring new key information regarding the evolution of permeability within the cohesive zone, between the onset and completion of strain localization in the rock. We find that transport properties are heterogeneous at the cm scale, and that the key driver for permeability evolution is the connectivity of subfaults. Remarkably, in this phase, permeability increases mostly at the onset of slip, within the first 100s of microns of displacement. Once a connected fault is formed, permeability is only weakly impacted by fault slip. These observations are consistent with recent measurements of local dilatancy in initially intact granite (Aben & Brantut, 2023), where dilatancy is shown to be most dramatic in the very early stages of deformation and fault growth.

5. Conclusions

We conducted rock fracture experiments under triaxial conditions, and used a combination of flow through tests monitored by internal pore pressure sensors and AE monitoring during loading to determine the gradual increase and heterogeneity in fluid transport properties from the intact rock until a through-going fault is formed. The main conclusions can be summarized as follows.

- During initial loading prior to peak stress, the average permeability increases dramatically, by up to two orders of magnitude.
- In the post-peak phase, during the formation of the fault zone, the average permeability increases approximately by a factor 3.
- Fault formation proceeds by the extension of fractures from the notches pre-cut in the sample. These initial fractures are not completely connected, which is reflected by the strong heterogeneity in hydraulic transmissivity in the sample. Unconnected regions retain a relatively lower transmissivity.
- The completion of the fault across the entire sample is marked by a relative homogenization of transmissivity. Fault completion is associated with a substantial shear stress drop. During that stage, some regions of the fault experience a local decrease in transmissivity.
- Continued slip on the newly formed fault is associated with net dilation, but hydraulic transmissivity is only weakly increasing.

Our results show a clear relationship between AE activity illuminating fracture growth, and the development of local permeability heterogeneities. This relationship, observed at the sample scale, is qualitatively consistent with seismological interpretations of the propagation of seismic swarms in the crust (e.g., De Barros et al., 2020; Ross & Cochran, 2021; Ross et al., 2020), and reinforces the hypothesis that swarms could be produced by migrating fluids, in a feedback between deformation-induced permeability increase, fluid flow and fault slip (e.g., Almakari et al., 2020).

The accurate determination of the full 3D dimensional evolution of permeability, and possibly its anisotropy, during faulting requires further work in two directions: (a) more experimental data exploring the role of confining pressure, pore pressure, with more internal pressure sensors to increase coverage, and (b) full 3D numerical simulations of fluid flow, and inversion of local permeability values from the combination of pore pressure records and fault geometry.

Appendix A: Numerical Flow Simulation in a Homogeneous Rock

Numerical fluid flow simulations were conducted by solving Equation 4 with the finite element method, using the software package Firedrake (Ham et al., 2023). The cylindrical sample of unit length was meshed (using GMSH (Geuzaine & Remacle, 2009),) into tetrahedral elements. The pressure distribution in the sample is dependent on relative permeability differences in the sample, not on the absolute permeability values. Hence, a normalized material permeability of 1 was used. To simplify meshing of the notches, they were simulated as a material with permeability 10^3 (we checked that this exact value did not interfere with the outcome of the simulation, as long as it was sufficiently large). The boreholes were explicitly meshed. Constant pore pressure boundary conditions were used at the top and bottom end of the sample, including along the borehole faces. We solved an uncoupled Darcy problem, under the assumption that the stress levels in the sample outside the fault zone remain constant throughout the 23 stages of the faulting process under consideration. Consequently, the fluid flow was computed within a rigid porous medium. A zero lateral flow condition was used along the sides of the cylinder. We used a mixed finite element method, where fluid velocity was discretized using Raviart-Thomas elements of degree 2, and pore pressure was discretized with discontinuous Galerkin elements of degree 1. A sensitivity analysis was conducted for the mesh size dependency of the simulation results, showing that variation in simulated flow rate and fluid pressure is well below 2% for the range of mesh sizes tested (Figure A1).

The simulation output with a homogeneous bulk permeability was used to extract the values of pore pressure (after appropriate scaling) as a function of position along the sample, reported as dashed lines in Figures 2, 3 and 7.

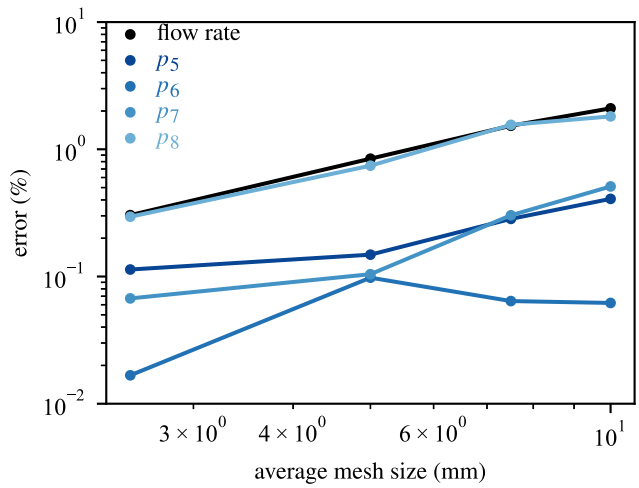

Figure A1. Relative error in flow rate and pressures at different sensor locations as a function of average meash size. The error is computed in reference to a computation performed with an average meash size of 1 mm.

Data Availability Statement

Data underlying the conclusions of this paper are available at Aben and Brantut (2024).

Acknowledgments
Neil Hughes provided technical support on the triaxial apparatus. Francesco Iacoviello performed the CT scans at UCL's Electrochemical Innovation Lab X-ray imaging facility. We acknowledge funding from the UK Natural Environment Research Council (grant NE/S000852/1) and the European Research Council under the European Union's Horizon 2020 research and innovation programme (project RockDEaF, grant agreement 804685).

References

Aben, F. M., & Brantut, N. (2021). Dilatancy stabilises shear failure in rock. *Earth and Planetary Science Letters*, *574*, 117–174. https://doi.org/10.1016/j.epsl.2021.117174

Aben, F. M., & Brantut, N. (2023). Rupture and after slip controlled by spontaneous local fluid flow in crustal rock. *Journal of Geophysical Research*, *128*(11), e2023JB027534. https://doi.org/10.1029/2023JB027534

Aben, F. M., & Brantut, N. (2024). Dataset for "permeability development during fault growth and slip in granite [1.0]" [Dataset]. https://doi.org/10.5281/zenodo.10854135

Aben, F. M., Brantut, N., Mitchell, T. M., & David, E. C. (2019). Rupture energetics in crustal rock from laboratory-scale seismic tomography. *Geophysical Research Letters*, *46*(13), 7337–7344. https://doi.org/10.1029/2019GL083040

Almakari, M., Chauris, H., Passelègue, F., Dublanchet, P., & Gesret, A. (2020). Fault's hydraulic diffusivity enhancement during injection induced fault reactivation: Application of pore pressure diffusion inversions to laboratory injection experiments. *Geophysical Journal International*, *223*(3), 2117–2132. https://doi.org/10.1093/gji/ggaa446

Boneh, Y., Chang, J. C., Lockner, D. A., & Reches, Z. (2014). Evolution of wear and friction along experimental faults. *Pure and Applied Geophysics*, *171*(11), 3125–3141. https://doi.org/10.1007/s00024-014-0801-3

Brace, W. F., & Byerlee, J. D. (1966). Stick-slip as a mechanism for earthquakes. *Science*, *153*(3739), 990–992. https://doi.org/10.1126/science.153.3739.990

Brace, W. F., Walsh, J. B., & Frangos, W. T. (1968). Permeability of granite under high pressure. *Journal of Geophysical Research*, *73*(6), 2225–2236. https://doi.org/10.1029/jb073i006p02225

Brantut, N. (2015). Time-dependent recovery of microcrack damage and seismic wave speeds in deformed limestone. *Journal of Geophysical Research*, *120*(12), 8088–8109. https://doi.org/10.1002/2015JB012324

Brantut, N. (2020). Dilatancy-induced fluid pressure drop during dynamic rupture: Direct experimental evidence and consequences for earthquake dynamics. *Earth and Planetary Science Letters*, *538*, 116–179. https://doi.org/10.1016/j.epsl.2020.116179

Brantut, N. (2021). Dilatancy toughening of shear cracks and implications for slow rupture propagation. *Journal of Geophysical Research*, *126*(11), e2021JB022239. https://doi.org/10.1029/2021JB022239

Brantut, N., & Aben, F. M. (2021). Fluid pressure heterogeneity during fluid flow in rocks: New laboratory measurement device and method. *Geophysical Journal International*, *225*(2), 968–983. https://doi.org/10.1093/gji/ggab019

Brener, E., & Bouchbinder, E. (2021). Theory of unconventional singularities of frictional cracks. *Journal of the Mechanics and Physics of Solids*, *153*, 104466. https://doi.org/10.1016/j.jmps.2021.104466

Chester, F. M., & Chester, J. S. (2000). Stress and deformation along wavy frictional faults. *Journal of Geophysical Research*, *105*(B10), 23421–23430. https://doi.org/10.1029/2000jb900241

Crawford, B. R., Faulkner, D. R., & Rutter, E. H. (2008). Strength, porosity, and permeability development during hydrostatic and shear loading of synthetic quartz-clay fault gouge. *Journal of Geophysical Research*, *113*(B3), B03207. https://doi.org/10.1029/2006JB004636

De Barros, L., Cappa, F., Deschamps, A., & Dublanchet, P. (2020). Imbricated aseismic slip and fluid diffusion drive a seismic swarm in the Corinth Gulf, Greece. *Geophysical Research Letters*, *47*(9), e2020GL087142. https://doi.org/10.1029/2020GL087142

Farquharson, J. I., Heap, M. J., & Baud, P. (2016). Strain-induced permeability increase in volcanic rock. *Geophysical Research Letters*, *43*(22), 11603–11610. https://doi.org/10.1002/2016gl071540

Faulkner, D. R., Sanchez-Roa, C., Boulton, C., & den Hartog, S. A. M. (2018). Pore fluid pressure development in compacting fault gouge in theory, experiments, nature. *Journal of Geophysical Research*, *123*(1), 226–241. https://doi.org/10.1002/2017JB015130

Garagash, D. I., & Rudnicki, J. W. (2003). Shear heating of a fluid-saturated slip-weakening dilatant fault zone 1. Limiting regimes. *Journal of Geophysical Research*, *108*(B2). https://doi.org/10.1029/2001jb001653

Geuzaine, C., & Remacle, J.-F. (2009). GMSH: A three-dimensional finite element mesh generator with built-in pre- and post-processing facilities. *International Journal for Numerical Methods in Engineering*, *79*(11), 1309–1331. https://doi.org/10.1002/nme.2579

Ham, D. A., Kelly, P. H. J., Mitchell, L., Cotter, C. J., Kirby, R. C., Sagiyama, K., et al. (2023). *Firedrake user manual* (1st ed.). Imperial College London and University of Oxford and Baylor University and University of Washington. https://doi.org/10.25561/104839

Im, K., Elsworth, D., & Fang, Y. (2018). The influence of preslip sealing on the permeability evolution of fractures and faults. *Geophysical Research Letters*, *45*(1), 166–175. https://doi.org/10.1002/2017GL076216

Kiyama, T., Kita, H., Ishijima, Y., Yanagidani, T., Aoki, K., & Sato, T. (1996). Permeability in anisotropic granite under hydrostatic compression and triaxial compression include post-failure region. In *2nd North American Rock Mechanics Symposium*.

Kluge, C., Blöcher, G., Barnhoorn, A., Schmittbuhl, J., & Bruhn, D. (2021). Permeability evolution during shear zone initiation in low-porosity rocks. *Rock Mechanics and Rock Engineering*, *54*(10), 5221–5244. https://doi.org/10.1007/s00603-020-02356-0

Lockner, D. A., Byerlee, J. D., Kuksenko, V., Ponomarev, A., & Sidorin, A. (1991). Quasi-static fault growth and shear fracture energy in granite. *Nature*, *350*(6313), 39–42. https://doi.org/10.1038/350039a0

Mitchell, T. M., & Faulkner, D. R. (2008). Experimental measurements of permeability evolution during triaxial compression of initially intact crystalline rocks and implications for fluid flow in fault zones. *Journal of Geophysical Research*, *113*(B11), B11412. https://doi.org/10.1029/2008JB005588

Moore, D. E., & Lockner, D. A. (1995). The role of microcracking in shear-fracture propagation in granite. *Journal of Structural Geology*, *17*(1), 95–111. https://doi.org/10.1016/0191-8141(94)e0018-t

Muir Wood, D. (1990). *Soil behaviour and critical state soil mechanics*. Cambridge University Press.

Ohnaka, M., & Shen, L. (1999). Scaling of the shear rupture process from nucleation to dynamic propagation: Implications of geometry irregularity of the rupturing surfaces. *Journal of Geophysical Research*, *104*(B1), 817–844. https://doi.org/10.1029/1998jb900007

Paglialunga, F., Passelègue, F. X., Brantut, N., Barras, F., Lebihain, M., & Violay, M. (2022). On the scale dependence in the dynamics of frictional rupture: Constant fracture energy versus size-dependent breakdown work. *Earth and Planetary Science Letters*, *584*, 117–442.

Rice, J. R. (2006). Heating and weakening of faults during earthquake slip. *Journal of Geophysical Research*, *111*(B5), B05311. https://doi.org/10.1029/2005JB004006

Ross, Z. E., & Cochran, E. S. (2021). Evidence for latent crustal fluid injection transients in Southern California from long-duration earthquake swarms. *Geophysical Research Letters*, *48*(12), e2021GL092465. https://doi.org/10.1029/2021GL092465

Ross, Z. E., Cochran, E. S., Trugman, D. T., & Smith, J. D. (2020). 3D fault architecture controls the dynamism of earthquake swarms. *Science*, *368*(6497), 1357–1361. https://doi.org/10.1126/science.abb0779

Rutter, E. H., & Mecklenburgh, J. (2018). Influence of normal and shear stress on the hydraulic transmissivity of thin cracks in a tight quartz sandstone, a granite, and a shale. *Journal of Geophysical Research*, *123*(2), 1262–1285. https://doi.org/10.1002/2017JB014858

Sleeman, R., & van Eck, T. (1999). Robust automatic P-phase picking: An on-line implementation in the analysis of broadband seismogram recordings. *Physics of the Earth and Planetary Interiors*, *113*(1–4), 265–275. https://doi.org/10.1016/s0031-9201(99)00007-2

Tapponnier, P., & Brace, W. F. (1976). Development of stress-induced microcracks in Westerly granite. *International Journal of Rock Mechanics and Mining Science & Geomechanics Abstracts*, *13*(4), 103–112. https://doi.org/10.1016/0148-9062(76)91937-9

Teufel, L. W. (1987). Permeability changes during shear deformation of fractured rock. In *28th U.S. Rock Mechanics/Geomechanics Symposium* (pp. 473–480). American Rock Mechanics Association.

Townend, J., & Zoback, M. D. (2000). How faulting keeps the crust strong. *Geology*, *28*(5), 399–402. https://doi.org/10.1130/0091-7613(2000)028<0399:hfktcs>2.3.co;2

Viesca, R. C., & Garagash, D. I. (2015). Ubiquitous weakening of faults due to thermal pressurization. *Nature Geoscience*, *8*(11), 875–879. https://doi.org/10.1038/ngeo2554

Walsh, J. B. (1981). Effect of pore pressure and confining pressure on fracture permeability. *International Journal of Rock Mechanics and Mining Science & Geomechanics Abstracts*, *18*(5), 429–435. https://doi.org/10.1016/0148-9062(81)90006-1

Wang, W., & Scholz, C. H. (1994). Wear processes during frictional sliding of rock: A theoretical and experimental study. *Journal of Geophysical Research*, *99*(B4), 6789–6799. https://doi.org/10.1029/93jb02875

Wong, T.-F. (1982). Shear fracture energy of Westerly granite from post-failure behavior. *Journal of Geophysical Research*, *87*(B2), 990–1000. https://doi.org/10.1029/jb087ib02p00990

Zang, A., Wagner, F. C., Stanchits, S., Janssena, C., & Dresen, G. (2000). Fracture process zone in granite. *Journal of Geophysical Research*, *105*(B10), 23651–23661. https://doi.org/10.1029/2000jb900239

Zhang, S., & Tullis, T. E. (1998). The effect of fault slip on permeability and permeability anisotropy in quartz gouge. *Tectonophysics*, *295*(1–2), 41–52. https://doi.org/10.1016/s0040-1951(98)00114-0

Zhang, S., Tullis, T. E., & Scruggs, V. J. (1999). Permeability anisotropy and pressure dependency of permeability in experimentally sheared gouge materials. *Journal of Structural Geology*, *21*(7), 795–806. https://doi.org/10.1016/s0191-8141(99)00080-2

Zoback, M. D., & Byerlee, J. D. (1975). The effect of microcrack dilatancy on the permeability of Westerly granite. *Journal of Geophysical Research*, *80*(5), 752–755. https://doi.org/10.1029/jb080i005p00752